

Article

Enhanced Electrochemical Performance of $\text{Li}_4\text{Ti}_5\text{O}_{12}$ by Niobium Doping for Pseudocapacitive Applications

Jinka Chandrasekhar ¹, Merum Dhananjaya ¹, Obili M. Hussain ^{1,*}, Alain Mauger ² and Christian M. Julien ^{2,*} 

¹ Thin film Laboratory, Department of Physics, Sri Venkateswara University, Tirupati 517502, India; jcsekhar4@gmail.com (J.C.); msdhananjaya51@gmail.com (M.D.)

² Institut de Minéralogie, de Physique des Matériaux et de Cosmochimie (IMPMC), Sorbonne Université, CNRS UMR 7590, 4 Place Jussieu, 75005 Paris, France; alain.mauger@sorbonne-universite.fr

* Correspondence: hussainsvu@gmail.com (O.M.H.); christian.julien@sorbonne-universite.fr (C.M.J.)

Abstract: Niobium-doped nanocrystalline $\text{Li}_4\text{Ti}_5\text{O}_{12}$ (LTO) is synthesized by the solid-state reaction method, and the influence of dopant concentration ($x = 2\text{--}10$ mol%) on microstructural and electrochemical properties is studied. The X-ray diffraction and Raman patterns assessed the cubic spinel structure of $\text{Li}_4\text{Ti}_{5-x}\text{Nb}_x\text{O}_{12}$ phase in all samples. Marginal changes in the lattice parameters, unit cell volume and dislocation density of LTO are observed with Nb substitution. The higher ionic radius of Nb induces a lattice expansion, which may be favorable for more ion intercalation/deintercalation. The SEM and TEM images display uniformly distributed nano-sized cubical particles. The represented (hkl) orientations of the SAED pattern and d-spacing (0.46 nm) between bright fringes confirm the well-crystallized LTO phase. The EDS and elemental mapping results demonstrate that Nb elements are uniformly doped in LTO with a proper stoichiometric ratio. The optimized 8%Nb-doped LTO electrode exhibits pseudocapacitive behavior and delivers a high specific capacitance of 497 F g^{-1} at a current density of 1 A g^{-1} with 92.3% of specific capacitance retention even after 5000 cycles.

Keywords: $\text{Li}_4\text{Ti}_5\text{O}_{12}$; Nb doping; nanostructure; supercapacitor; energy storage



Citation: Chandrasekhar, J.; Dhananjaya, M.; Hussain, O.M.; Mauger, A.; Julien, C.M. Enhanced Electrochemical Performance of $\text{Li}_4\text{Ti}_5\text{O}_{12}$ by Niobium Doping for Pseudocapacitive Applications. *Micro* **2021**, *1*, 28–42. <https://doi.org/10.3390/micro1010004>

Academic Editor: Hiroshi Furuta

Received: 2 May 2021

Accepted: 2 June 2021

Published: 4 June 2021

Publisher's Note: MDPI stays neutral with regard to jurisdictional claims in published maps and institutional affiliations.



Copyright: © 2021 by the authors. Licensee MDPI, Basel, Switzerland. This article is an open access article distributed under the terms and conditions of the Creative Commons Attribution (CC BY) license (<https://creativecommons.org/licenses/by/4.0/>).

1. Introduction

The demand for electrochemical energy storage (EES) devices has grown day by day considering their potential applications in various electronic products ranging from toys to submarines. Among these devices, supercapacitors have been established as one of the proficient energy storage systems due to their high-power density, fast charge/discharge capability, and comprehensive cycle life properties [1,2]. The electrochemical activity of the supercapacitors relies effectively on the charge conservation of active electrode materials (carbon, metal oxides, and conducting polymers) [3–6]. Essentially, the transition-metal oxides (TMOs) progressed as favorable electrode materials due to excellent structural stability during the electrochemical reaction, as well as the fact that they are plentiful and less expensive. Moreover, several researchers have stated that TMO electrodes exhibit either capacitive/faradaic reactions or both and are ideal for the application of electrochemical double layer capacitors (EDLCs) or pseudocapacitors (PCs) [7–11]. Besides supercapacitors and batteries, the hybrid devices are an interesting combination of both devices [12].

Among all TMOs, the cubic spinel $\text{Li}_4\text{Ti}_5\text{O}_{12}$ (LTO) is one of the potential candidates for EES applications due to its outstanding cycle life and zero strain property during the charging/discharging process. It delivers a high theoretical capacity of 175 mAh g^{-1} since three or more Li^+ ions are accommodated per one formula unit. Moreover, a flat discharge profile at 1.55 V (vs. Li^+/Li) demonstrates that it avoids the formation of SEI film. However, the LTO is a large bandgap (3.54 eV) semiconductor, in which the electrons are transferred from the $3d$ state of Ti to the $2p$ states of O, which leads to low electrical conductivity ($10^{-13}\text{--}10^{-9} \text{ S cm}^{-1}$) and limits the electrochemical activity [13–16]. Several

innovative methodologies have been used to solve these challenges, such as the preparation of nano-sized particles, surface coating or composing with carbon materials, doping with metallic elements, etc. The coating of LTO with a conductive material improves electrical contact between particles but has no effect on lithium-ion diffusivity. On the other hand, both the lattice electronic conductivity and lithium-ion diffusivity can be strengthened by doping with metal ions (Cr^{3+} , V^{5+} , Ta^{5+} , Co^{3+} , Cu^{2+} , Ga^{3+} , Sc^{3+} , Fe^{3+} , Mg^{2+} , Mn^{4+} , and Nb^{5+}) in Li or Ti sites [17–28].

Ji et al. reported the co-doping of La^{3+} and F^- ions in LTO, which provides a high amount of $\text{Ti}^{3+}/\text{Ti}^{4+}$ charge compensation resulting in improvement in both the electronic conductivity and diffusivity of the lithium ion [29]. Tian et al. investigated the electrochemical behavior of prepared $\text{Li}_4\text{Ti}_5\text{Nb}_{0.05}\text{O}_{12}$ electrodes in the potential range of 0–2.5 V and showed that the Nb-doping increased the specific capacity and cycling stability [30]. Jeong et al. fabricated pure and different valence-state metal-ion-doped LTO electrodes using the solid-state reaction method. The microstructural and electrochemical analyses demonstrated that metal-ion-doped LTO materials are promising electrodes for LIB applications [31].

Several reports are related to the electrochemical performance of LTO-based composites as anode materials for asymmetric supercapacitors, including LTO confined in carbon nanopores [32], LTO/MWCNT hybrid [33], sol-gel prepared LTO [34], graphene-modified LTO [35], porous LTO granules [36], and LTO sintered at 1000 °C [37]. Only two studies examined the capacitive properties of doped LTO powders. LTO doped with various dopants (Al^{3+} , Cr^{3+} , Mg^{2+}) synthesized by solid-state reaction have been investigated as electrodes of hybrid supercapacitors, but the reported characteristics are limited [38,39]. Lee et al. reported an enhancement in the electronic conductivity of $\text{Li}_4\text{Ti}_5\text{O}_{12}$ by doping with Mg^{2+} and Cr^{3+} , which improved the electrochemical behavior for hybrid supercapacitor applications [38]. Khairy et al. [39] synthesized lithiated $\text{Li}_{4+x}\text{M}_{0.1}\text{Ti}_{4.9}\text{O}_{12}$ ($M = \text{Mg}, \text{Mn}$ and V) materials using a conventional solid-state reaction. Specific capacitances of 184, 202 and 223 F g^{-1} were obtained from cyclic voltammetry measurements at a 5 mV s^{-1} scan rate for Mg-, Mn- and V-doped LTO, respectively. Some work reported the electrochemical performance of Nb-doped LTO as anode material for Li-ion batteries. Sarantuya et al. calculated the effect of Nb, Cr, and Fe doping on the electronic structure of LTO using density functional theory and found that Nb-doped should be preferred [40]. Tian et al. [41] reported that $\text{Li}_4\text{Ti}_{4.95}\text{Nb}_{0.05}\text{O}_{12}$ exhibits a higher electronic conductivity and faster lithium-ion diffusivity than the LTO, delivering a specific capacity of 135 mAh g^{-1} at 10C rate. Similar values were reported by Shi et al. [16], who state that the Nb-doped LTO electrode with the Nb concentration of $x = 0.03$ exhibits the best electrochemical performance. Yi et al. [42] assumed that Nb^{5+} ions substitute for Ti^{4+} with very few oxygen vacancies in the $\text{Li}_4\text{Ti}_{4.95}\text{Nb}_{0.05}\text{O}_{12}$ spinel, thus explaining the higher electrical conductivity. Moreover, Nb has a higher ionic radius (0.69 Å) than Ti or Li so that Nb-doping also increases the lattice parameter, which may benefit the Li^+ conductivity, while maintaining the structure stability during the electrochemical reactions. However, Nb-doped $\text{Li}_4\text{Ti}_5\text{O}_{12}$ was not applied as electrode material of supercapacitors so far.

In this work, the analyses are intended to improve the microstructural and electrochemical properties of LTO by doping with Nb^{5+} . The Nb-doped $\text{Li}_4\text{Ti}_5\text{O}_{12}$ nanopowders were successfully synthesized by a simple solid-state reaction method. $\text{Li}_4\text{Ti}_{5-x}\text{Nb}_x\text{O}_{12}$ samples with composition in the range $0.0 \leq x \leq 0.1$ are investigated. Structural and morphological characteristics are investigated by X-ray diffraction (XRD), Raman scattering (RS) spectroscopy, scanning electron microscopy (SEM), and high-resolution transmission electron microscopy (HRTEM), selected area electron diffraction (SAED), respectively. Electrochemical properties were investigated by means of cyclic voltammetry (CV) galvanostatic charge–discharge (GCD) titration, and electrochemical impedance spectroscopy (EIS). The influence of Nb in the 2–10% doping range on electrochemical properties are studied, and their suitability for use as electrodes for pseudocapacitors is demonstrated.

2. Materials and Methods

Lithium carbonate (Li_2CO_3) (99.99%, trace metal basis), titanium (IV) oxide, anatase (TiO_2) (99.8%, trace metals basis), niobium (V) oxide (Nb_2O_5) (99.99%, trace metals basis), lithium sulfate (Li_2SO_4) ($\geq 99.99\%$, trace metals basis), polyvinylidene fluoride (PVDF) binder, and N-methyl-2-pyrrolidone ($\geq 99\%$, ACS reagent) were purchased from Sigma Aldrich (Taufkirchen, Germany) and used without further purifications.

$\text{Li}_4\text{Ti}_{5-x}\text{Nb}_x\text{O}_{12}$ powders ($0.0 \leq x \leq 0.1$) were synthesized by the solid-state reaction method. The stoichiometric amounts of Li_2CO_3 , TiO_2 and Nb_2O_5 were used as precursor materials. The mixture of raw materials was ground for 3 h with a sufficient amount of ethanol poured into the powder. The obtained slurry was placed in a micro-oven and dehydrated at 80°C for 5 h. Further, the powders were sintered in a furnace at an optimized temperature of 900°C for 5 h in air. The crystallographic structures of prepared Nb-doped $\text{Li}_4\text{Ti}_5\text{O}_{12}$ powders were analyzed by X-ray diffractometry (XRD, Siefert—303 TT diffractometer). The XRD spectra were recorded with the Cu-K α radiation source ($\lambda = 0.15406\text{ nm}$) in the angular 2θ range from 10° to 70° at a scan rate of 1° min^{-1} . The structural analysis of $\text{Li}_4\text{Ti}_{5-x}\text{Nb}_x\text{O}_{12}$ powders was also performed by Raman spectroscopy utilizing a LabRAM-HR 800 confocal apparatus (Horiba, Kyoto, Japan) equipped with a He Ne laser (632 nm as excitation wavelength). The microstructure and morphology of synthesized powders were characterized by HRTEM and SEM using a HRTEM-FEI microscope (TECHNAIG2-30S-twin D905) and a SEM microscope (Carl Zeiss EVO50), respectively. The elemental composition of the synthesized $\text{Li}_4\text{Ti}_5\text{O}_{12}$ powder was analyzed by an energy dispersive spectrometer attached in the TEM column.

The electrochemical properties of the synthesized Nb-doped LTO samples were studied using a three-electrode aqueous glass cell composed of platinum plate ($>99.95\%$, 10 mm \times 20 mm \times 0.5 mm, Latech) as the counter electrode, Ag/AgCl (+0.195 V vs. RHE, Allum Co., Kissimmee, FL, USA, model RE-1S) as the reference electrode and Nb-doped $\text{Li}_4\text{Ti}_5\text{O}_{12}$ as the working electrode. The working electrode loading was $\sim 1.5\text{ mg cm}^{-2}$. The working electrode was made by the doctor blade method using the active material (wt. 80%) mixed with a conducting agent, i.e., acetylene black (wt. 10%), and a binder, i.e., polyvinylidene fluoride (wt. 10%), which are used to enhance the electronic conductivity [43]. The mixture was added with a few drops of N-methyl-2-pyrrolidone to form a slurry and deposited on the Ni substrates. The electrode was dried at 100°C for 1 h on a hot plate, then placed in a furnace at 200°C for 3 h. The electrochemical performance of the prepared samples was conducted in the 1 mol L^{-1} saturated lithium sulfate (electrolyte) aqueous solution. The cyclic voltammetry and galvanostatic charge–discharge were conducted at room temperature with a CHI 608C electrochemical workstation in the potential window ranging from -0.3 V to $+0.5\text{ V}$ vs. Ag/AgCl. Moreover, EIS data were recorded using a CHI 608C electrochemical workstation in the frequency from 1 MHz to 1 Hz at corresponding open-circuit potentials.

3. Results

3.1. Structure and Morphology of Nb-Doped LTO

Figure 1a shows the X-ray diffraction patterns of $\text{Li}_4\text{Ti}_{5-x}\text{Nb}_x\text{O}_{12}$ ($0.0 \leq x \leq 0.1$). The diffraction peaks of pure and Nb-doped LTO powders are ascribed to the cubic spinel structure of $\text{Li}_4\text{Ti}_5\text{O}_{12}$ (JCPDS No. 49-0207) with the $Fd\bar{3}m$ space group [44,45]. No reflections due to impurities can be observed in the doping range 2–8%, indicating that Nb^{5+} ions are successfully incorporated into the lattice of $\text{Li}_4\text{Ti}_5\text{O}_{12}$ without rescinding the structure or producing a new phase when $x < 0.1$. However, several impurity phases, such as $\text{Li}_2\text{Ti}_3\text{O}_7$ and TiO_2 , can be observed at $x = 0.1$, which can thus be considered as the limit of solubility of Nb in LTO. The predominant (111) reflection and other typical planes of the spinel phase specify the crystalline nature of the synthesized powders. Figure 1b shows the enlarged view of the (111) crystalline plane in the range $17.5^\circ \leq 2\theta \leq 19.5^\circ$, giving evidence of a slight shift of (111) orientation to lower diffraction 2θ angles with increasing the molar ratio of Nb^{+5} from 0 to 8%, which infers that Nb^{+5} ions are introduced in the

LTO lattice. This result confirms no modification in the structure but a change of the cubic parameter. With the increasing Nb doping molar ratio, the calculated lattice parameters (Table S1 in Supplementary Materials) are slightly higher than that of the pristine LTO.

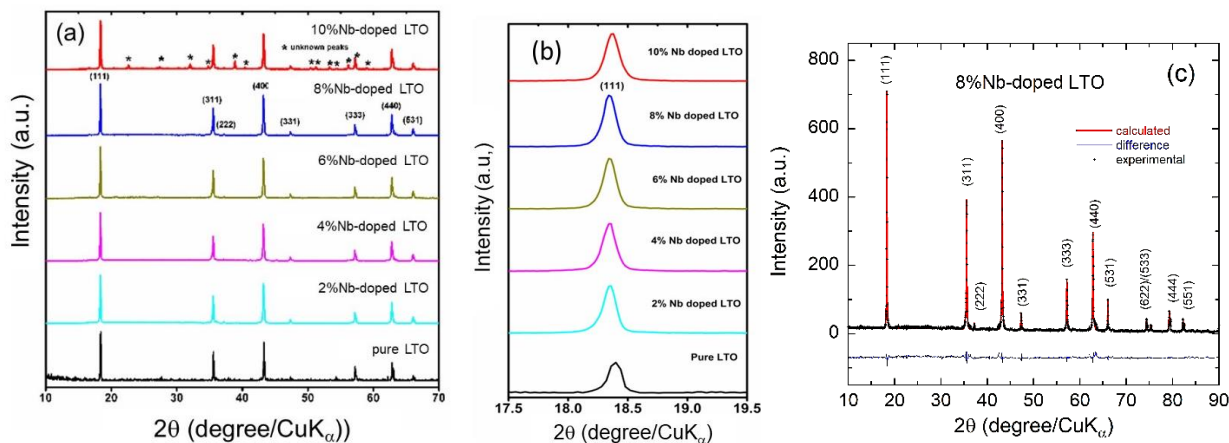


Figure 1. (a) XRD patterns of the Nb-doped $\text{Li}_4\text{Ti}_5\text{O}_{12}$ powders synthesized by solid-state reaction. (b) Enlarged (111) reflection. (c) Rietveld refinement of the 8%Nb-doped LTO sample. Stars indicate the peaks from impurities in the 10%Nb-doped LTO sample.

The Rietveld refinement profile of 8%Nb-doped LTO is shown in Figure 1c and the atomic site occupancies are listed in Table S2 in Supplementary Materials. XRD analysis and Rietveld refinement demonstrate that traces of the doped Nb^{5+} ions have successfully entered the lattice structure of the bulk LTO and the Nb doping does not change the spinel structure of LTO. Best fit was obtained by substituting Nb for Ti into the octahedral $16d$ sites. The cubic spinel Nb-doped LTO structure can be described in terms of the notation of $[\text{Li}_3]_{8a}[\text{LiTi}_{4.92}\text{Nb}_{0.08}]_{16d}[\text{O}_{12}]_{32e}$ within the $Fd\bar{3}m$ space group.

From previous literatures, M^{5+} doped ($M = \text{Nb}, \text{Ta}$) had been widely proved for improving physical and chemical properties of LTO owing to the significant effects of the metal ion dopants on their inner electronic and crystalline structure. Nb dopants with a valence 5+ and similar ionic radii (0.69 Å) as Ti^{4+} (0.68 Å) are considered to be reasonable solubility in Ti sites [30].

Crystallite size and dislocation density were extracted from XRD patterns (Table S1). The crystallite size (L) was calculated using the Debye–Scherrer formula (1) [46]:

$$L = \frac{K\lambda}{B \cos \theta}, \quad (1)$$

where K is a dimensionless shape factor (0.9 for quasi-spherical particles), λ is the wavelength of the X-ray source, B is the full width at half maximum (FWHM), and θ is the Bragg angle. The dislocation density (d) indicating the density of defects in the films was calculated using the following equation (2) [46]:

$$\delta = \frac{1}{L^2}, \quad (2)$$

The surface morphology of pure and $\text{Li}_4\text{Ti}_{5-x}\text{Nb}_x\text{O}_{12}$ ($0.00 \leq x \leq 0.1$) nanopowders was recorded using SEM and presented in Figure 2a–f. It can be clearly observed that the prepared samples are well crystallized with well-faced grains. Moreover, the morphology of the images is maintained in cubical shape with a random size distribution even at high doping concentration. The particle size distributions of the synthesized pure and Nb-doped LTO samples are illustrated in statistical histograms and shown in Figure 3a–f. All the LTO samples show a heterogeneous or random size distribution of particles in the nanoscale range. The size distribution of pure LTO powders is in the range 200–900 nm, with a

maximum at 450–500 nm. Only a few particles agglomerate, giving a finite size distribution above 750 nm. By increasing the Nb-doping from 2% to 8%, the maximum is shifted to smaller size, at 250 nm for $x = 0.08$.

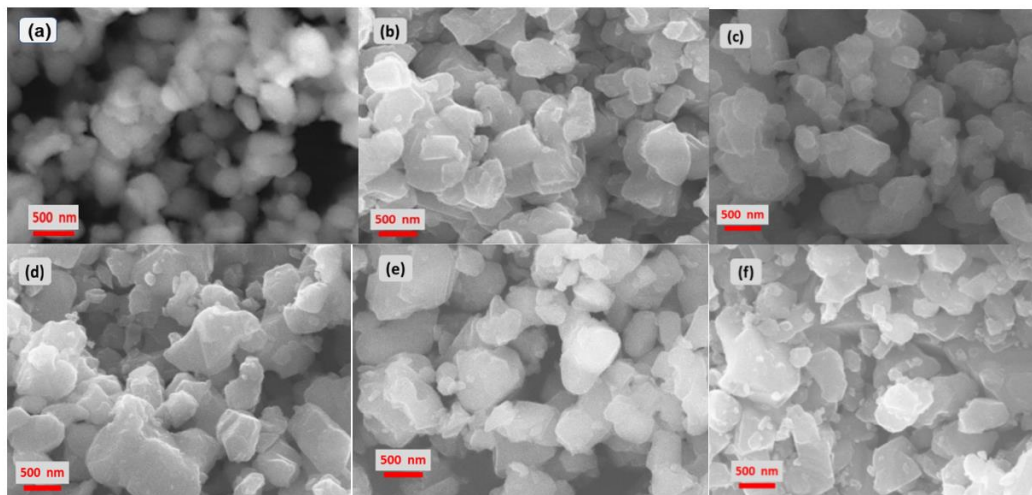


Figure 2. SEM images of (a) pure and (b–f) Nb-doped LTO samples: (b) 2%, (c) 4%, (d) 6%, (e) 8%, and (f) 10%. Note that particle sizes of Nb-doped LTO are comparable to that of pure LTO.

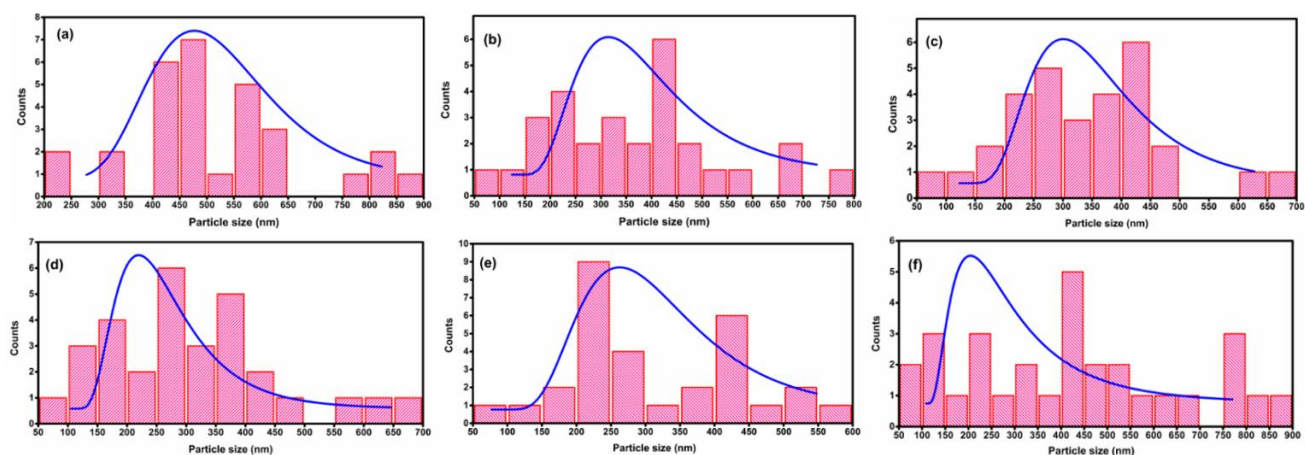


Figure 3. Statistical histogram for distribution of particle size of (a) pure and (b) 2%, (c) 4%, (d) 6%, (e) 8%, and (f) 10% Nb-doped $\text{Li}_4\text{Ti}_5\text{O}_{12}$ samples.

The chemical composition of the $\text{Li}_4\text{Ti}_{4.92}\text{Nb}_{0.08}\text{O}_{12}$ electrode was characterized by energy dispersive X-ray analysis as depicted in Figure 4. The oxygen, titanium, and niobium elemental peaks appear at energy levels of 0.154, 4.536, and 2.167 keV, respectively. The peak of the lithium element cannot appear from the EDAX spectrum because it has very low emission energy. The observed atomic percentages of Ti, O, and Nb elements of the (8%Nb-doped LTO) sample are 29.04, 69.84 and 1.12, in agreement with the chemical formula. The elemental mapping of $\text{Li}_4\text{Ti}_{4.92}\text{Nb}_{0.08}\text{O}_{12}$ is presented in Figure 5, showing that the Ti, O, and Nb elements are uniformly distributed in the compound. Since this is the highest level of doping below the limit of solubility of Nb, attention in the following will be focused on this composition.

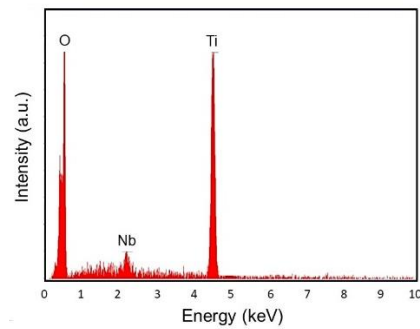


Figure 4. EDAX spectrum for element analyses of the $\text{Li}_4\text{Ti}_{4.92}\text{Nb}_{0.08}\text{O}_{12}$ sample.

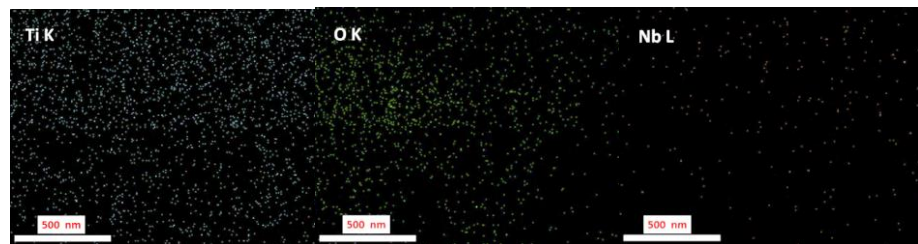


Figure 5. Elemental mapping of Ti, O, and Nb elements of the $\text{Li}_4\text{Ti}_{4.92}\text{Nb}_{0.08}\text{O}_{12}$ sample.

Figure 6a–c presents the HRTEM images and SAED patterns of the $\text{Li}_4\text{Ti}_{4.92}\text{Nb}_{0.08}\text{O}_{12}$ sample. Figure 6a displays uniform cubical structured particles and each particle contains different domains. The d -spacing was calculated from the distance between two bright fringes in the HRTEM image (Figure 6b) using the Image-J software. The obtained d -spacing values are found to be 0.484 and 0.296 nm corresponding to the (111) and (220) planes, respectively. The bright spots observed in the SAED pattern of $\text{Li}_4\text{Ti}_{4.92}\text{Nb}_{0.08}\text{O}_{12}$ powder (Figure 6c) indicate the good crystallinity of the prepared sample. Moreover, the (hkl) planes of the different spots analyzed using the Image-J software are attributed to the (111), (311), (400), (333), and (440) planes of the LTO spinel lattice. Obviously, the small increase in the d -spacing values from the HRTEM, and the SAED pattern of the synthesized powders, gives evidence of the slight increase in the lattice parameters, in agreement with the analysis of XRD spectra. These results confirm that the $\text{Li}_4\text{Ti}_{4.92}\text{Nb}_{0.08}\text{O}_{12}$ retains the spinel $\text{Li}_4\text{Ti}_5\text{O}_{12}$ -like phase.

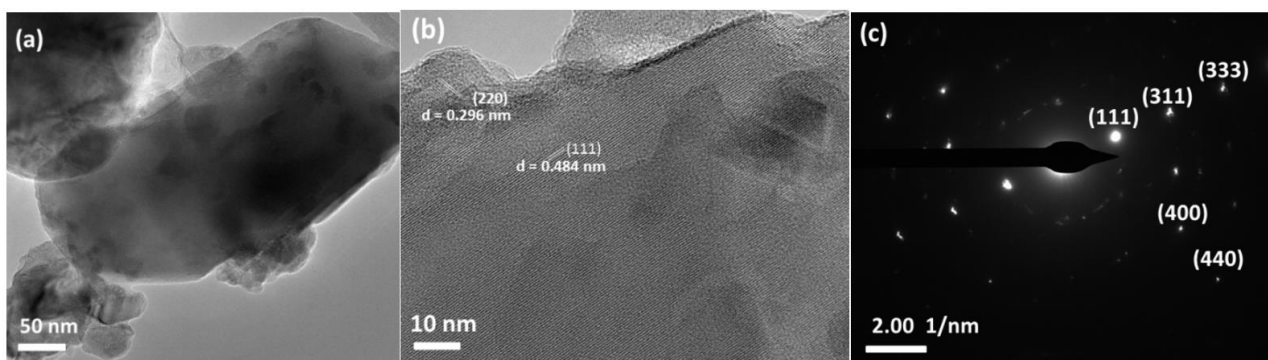


Figure 6. (a,b) HRTEM images and (c) SAED pattern of $\text{Li}_4\text{Ti}_{4.92}\text{Nb}_{0.08}\text{O}_{12}$ sample.

Figure 7 presents the Raman spectra of pure and $\text{Li}_4\text{Ti}_{4.92}\text{Nb}_{0.08}\text{O}_{12}$ samples recorded in the $100\text{--}1000\text{ cm}^{-1}$ spectral range. LTO spinel exhibits six Raman active modes ($3F_{2g} + 1E_g + 2A_{1g}$) [47], which are observed for both samples and located at 228, 253, 366, 418–430, 670, and 755 cm^{-1} , respectively. The high peak in the low frequency at 228 cm^{-1} corresponds to the bending vibrations of O–Ti–O bonds (F_{2g} mode). A weak Raman

peak observed at 253 cm^{-1} is associated to the F_{2g} mode. In the mid-frequency region, two peaks located at 366 and $418\text{--}430\text{ cm}^{-1}$ can be ascribed to the stretching vibrations of the Li-O bonds in LiO_4 (F_{2g} mode) and LiO_6 polyhedra (E_g mode), respectively. The peak at 670 cm^{-1} (A_{1g} mode) with a shoulder at 755 cm^{-1} (A_{1g} mode) is attributed to the vibrations of Ti-O bonds in TiO_6 octahedra. However, a shift (from 418 to 430 cm^{-1}) of peaks associated to Li-O bonds in LiO_6 polyhedra was observed when the doping concentration of Nb^{5+} increases from 0 to 8%. The red shift of the peak represents a weakening of the Li-O bond in $\text{Li}_4\text{Ti}_{5-x}\text{Nb}_x\text{O}_{12}$ samples, linked to the increase in the lattice parameters in the crystal. Moreover, no change in the peak position of 228 cm^{-1} corresponding to the O-Ti-O symmetric stretching mode is observed, which gives evidence of the structural stability of Nb-doped $\text{Li}_4\text{Ti}_5\text{O}_{12}$.

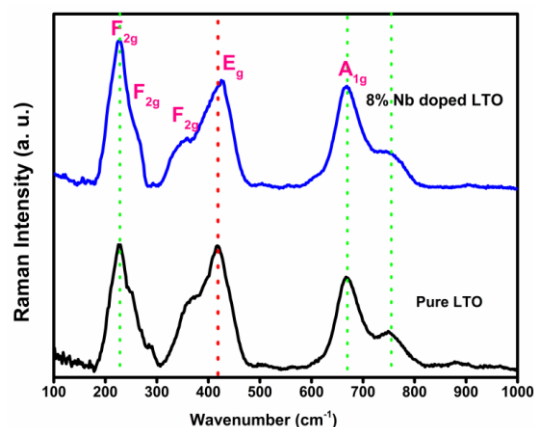


Figure 7. Raman scattering spectra of pure and $\text{Li}_4\text{Ti}_{4.92}\text{Nb}_{0.08}\text{O}_{12}$ samples.

The electrical conductivity of 8%Nb-doped LTO is found to be $2.37 \times 10^{-6}\text{ S cm}^{-1}$, which is higher than that of the pure LTO ($4.6 \times 10^{-9}\text{ S cm}^{-1}$). This motivated the study of the $\text{Li}_4\text{Ti}_{4.92}\text{Nb}_{0.08}\text{O}_{12}$ as an electrode for the pseudocapacitive application.

3.2. Electrochemical Performance

The significant variances in the electrochemical behavior of the Nb-doped LTO electrodes are clearly observed by the shape of the CV curves in the potential window of -0.3 to 0.5 V at a scan rate of 100 mV s^{-1} (Figure 8). With increasing Nb substitution from 2 to 8%, the typical charge–discharge curves change from a rectangular shape without redox peaks to a quasi-rectangular shape with anodic/cathodic peaks. Moreover, current densities are increased with increasing the Nb concentration in the LTO framework. When the doping concentration increases to 10%, the anodic/cathodic peaks are suppressed. This negative impact on the lithiation process may be the conduction band filled with more n-type Nb^{5+} ions and the less electroactive Ti^{4+} centers. In addition, the shape of charge–discharge curves shows a shift from pseudocapacitive to a battery-like profile induced by the Nb doping, associated to an increase in the electronic conductivity. The 8%Nb-doped LTO presents good oxidation–reduction curves with broad anodic/cathodic peaks of higher current densities and lower peak potential separation (0.33 V) than the other electrodes, confirming that the optimized $\text{Li}_4\text{Ti}_{4.92}\text{Nb}_{0.08}\text{O}_{12}$ electrode displays the highest electrochemical activity.

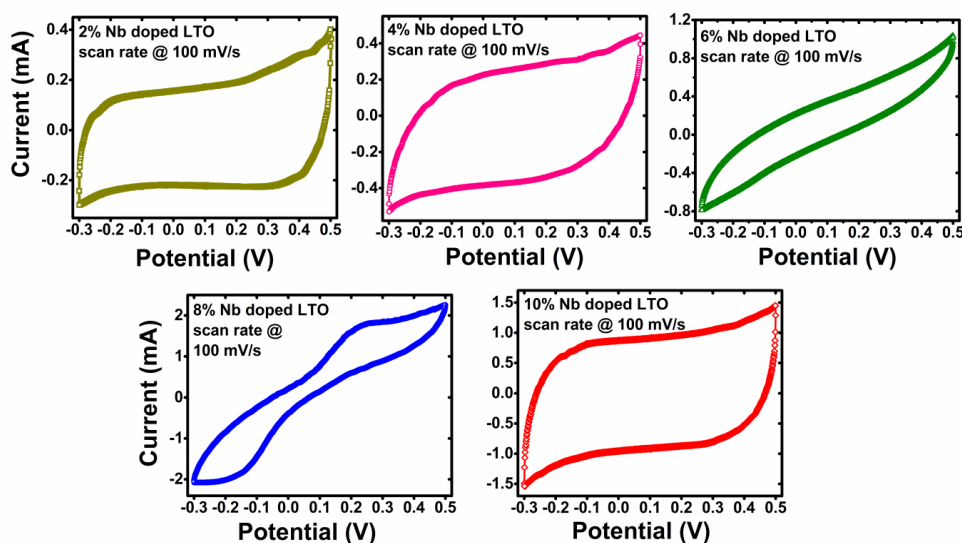


Figure 8. CV curves of $\text{Li}_4\text{Ti}_{5-x}\text{Nb}_x\text{O}_{12}$ ($0.02 \leq x \leq 0.10$) samples at a scan rate of 100 mV s^{-1} .

Figure 9a presents the cyclic voltammograms of the $\text{Li}_4\text{Ti}_{4.92}\text{Nb}_{0.08}\text{O}_{12}$ electrode in the voltage region of -0.3 to 0.5 V at different scan rates in the range 5 – 100 mV s^{-1} . All CV curves show a nonrectangular shape with broad anodic/cathodic peaks corresponding to a pseudocapacitive charge storage process [48]. The integral area of the CV curve proportionally increases with the increasing scan rate, and the positions of the anodic/cathodic peaks are marginally shifted. These results suggest an improvement in the reversibility of the redox reactions from the electrode. The charge storage mechanism on the surface of the electrodes influenced by the crystallite size, phase, and composition can be deduced from the exponent α of the power law $i_p = K\nu^\alpha$, which relates the peak current (i_p) of the CV curve to the scan rate (ν): $\alpha = 0.5$ indicates a diffusion charge storage control, and $\alpha = 1$ means a pure capacitive storage mechanism [49]. The value of $\alpha \approx 0.63$ deduced from the plot of $\log i_p$ vs. $\log \nu$ (Figure 9b) gives evidence that the charge storage is pseudocapacitive with both diffusion-controlled and capacitive-storage processes [50].

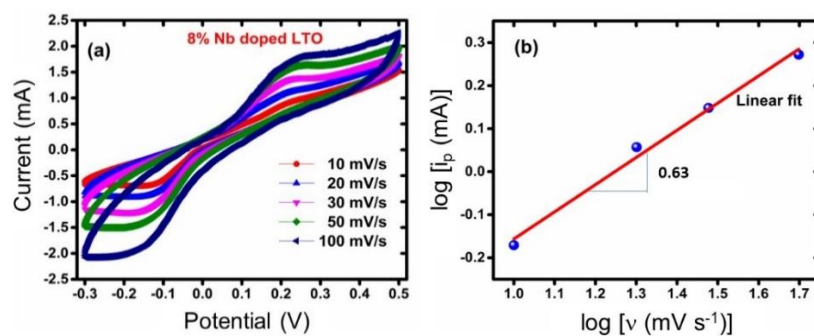


Figure 9. (a) CV curves of $\text{Li}_4\text{Ti}_{4.92}\text{Nb}_{0.08}\text{O}_{12}$ sample at various scan rates and (b) $\log i_p$ vs. $\log \nu$ graph.

The galvanometric charge–discharge (GCD) voltage curves of the Nb-doped LTO electrodes were studied using the chronopotentiometry technique at a current density of 2 A g^{-1} in the potential range of -0.3 to $+0.5 \text{ V vs. Ag/AgCl}$. The results are shown in Figure 10a–e, in which the dashed lines represent the charge/discharge behavior of an ideal capacitor. It is evidenced that LTO electrodes doped with 2%, 4%, and 10% Nb show an almost linear discharge profile. In contrast, the lineament of the GCD curves of 6% and 8% Nb-doped samples indicates that charges are partially intercalated/de-intercalated into/from the surface of the electrode like pseudocapacitive charge storage reactions, which

is consistent with the CV profiles (Figure 8 and Figure S1 in Supplementary Materials). GCD profiles display a shift from pseudocapacitive to battery-like behavior induced by Nb doping. The specific capacity of the $\text{Li}_4\text{Ti}_{5-x}\text{Nb}_x\text{O}_{12}$ pseudocapacitive electrodes are 39.4, 57.5, 95.8, 111.1 and 60.2 mAh g^{-1} for $x = 0.02, 0.04, 0.06, 0.08$ and 0.10, respectively, at a given current density of 2 A g^{-1} . Additionally, the 8%Nb-doped LTO delivered specific capacities of 138 and 75 mAh g^{-1} at current densities of 1 and 4 A g^{-1} . The coulombic efficiency of the prepared 2%, 4%, 6%, 8%, and 10%Nb-doped LTO electrodes was found to be 55.7%, 69%, 79.2%, 98.5% and 42.3%, respectively (see Figure S2 in Supplementary Materials).

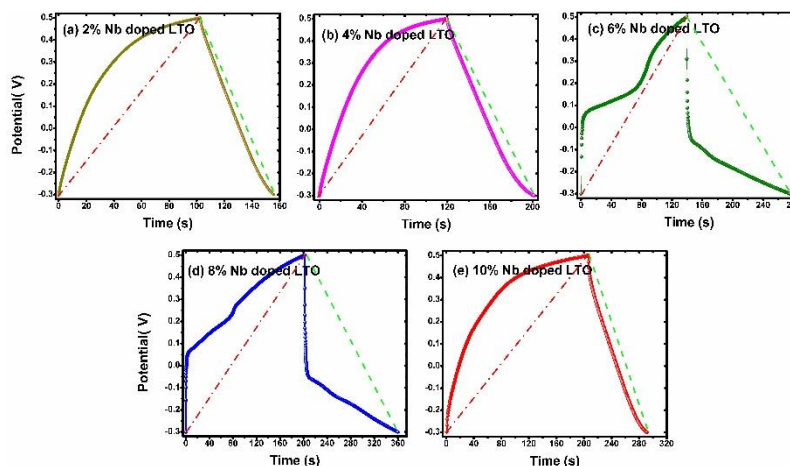


Figure 10. GCD curves of Nb-doped LTO electrodes recorded at current density of 2 A g^{-1} : (a) 2%, (b) 4%, (c) 6%, (d) 8% and (e) 10% Nb.

It appears that the $\text{Li}_4\text{Ti}_{4.92}\text{Nb}_{0.08}\text{O}_{12}$ electrode is discharged over a longer time than other electrodes, proving the higher electrochemical capability of the charge storage. The calculated specific capacitances of the $\text{Li}_4\text{Ti}_{5-x}\text{Nb}_x\text{O}_{12}$ electrodes are found to be 142, 207, 345, 400, and 217 F g^{-1} for $x = 0.02, 0.04, 0.06, 0.08$ and 0.1, respectively, at a given current density of 2 A g^{-1} (Figure 11), which illustrates the improvement in the electrochemical behavior of the electrodes with increasing the niobium concentration from 0.02 to 0.08.

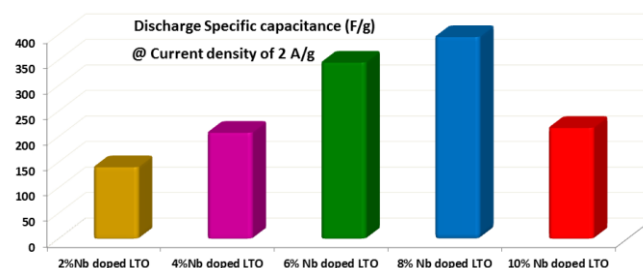


Figure 11. Comparison of the specific capacitances of Nb-doped LTO electrodes at 2 A g^{-1} .

Figure 12a presents the GCD profiles of the $\text{Li}_4\text{Ti}_{4.92}\text{Nb}_{0.08}\text{O}_{12}$ electrode carried out at current densities of 1, 2 and 4 A g^{-1} . At lower current, more charges participate in the electrochemical reactions, while a low number of charges contribute at higher current densities due to time constraints. The calculated specific capacitance of the electrode was found to be 497, 400, and 270 F g^{-1} at applied current densities of 1, 2, and 4 A g^{-1} , respectively. Correspondingly, the cycling stability of the $\text{Li}_4\text{Ti}_{4.92}\text{Nb}_{0.08}\text{O}_{12}$ electrode was studied over 5000 charge–discharge cycles as shown in Figure 12b. The capacitance retention is 92.3% at a current density of 1 A g^{-1} after 5000 cycles.

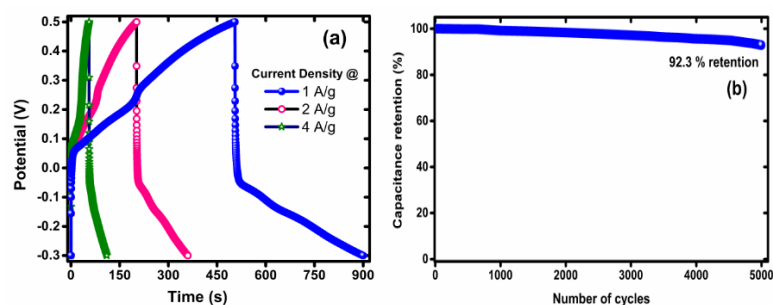


Figure 12. (a) The GCD profiles of the $\text{Li}_4\text{Ti}_{4.92}\text{Nb}_{0.08}\text{O}_{12}$ electrode at different applied currents in the range 1–4 A g^{-1} . (b) The cyclability over 5000 cycles at 1 A g^{-1} current rate.

The charge storage mechanism of the electrode significantly depends on the electrode internal resistance, electrolyte resistance, and interface resistance between electrode and electrolyte. These are determined from the Nyquist plots of the synthesized electrodes shown in Figure 13 along with the equivalent circuit composed of a series of resistances (R_s), which corresponds to the internal resistance of the cell (i.e., electrolyte and electrodes contribution), a charge transfer resistance (R_{ct}) in parallel with a constant phase element (CPE) and a Warburg element (inset of Figure 13). In the high-frequency region, R_s and R_{ct} of the electrodes were observed from the intercept of the x -axis and the diameter of the semicircle, respectively, while the Warburg impedance ($Z_w \approx \sigma_w \omega^{-1/2}$) of the element W is determined by the slope in the low-frequency region. The obtained R_s , R_{ct} and σ_w values for pristine and Nb-doped LTO electrodes are listed in Table 1. Values are decreased when increasing the doping percentage of niobium from 2 to 8% and then increased. This may be due to an increase in lattice parameter by increasing the doping percentage and hence improves electron mean free path and contact area between the electrode and electrolyte. Note the slight difference between R_s values (31.0 Ω vs. 18.1 Ω) is due to the high ohmic resistivity of pristine LTO compared with the doped electrode. The Warburg part shows an identical slope for $x = 8\%$ and $x = 2\%$, which suggests that the diffusion coefficient of Li is not affected by the doping. It, therefore, seems that the effect of doping is only the increase in electrical conductivity, which is not surprising, due to the small variation of the crystalline parameter and the absence of lithium vacancies.

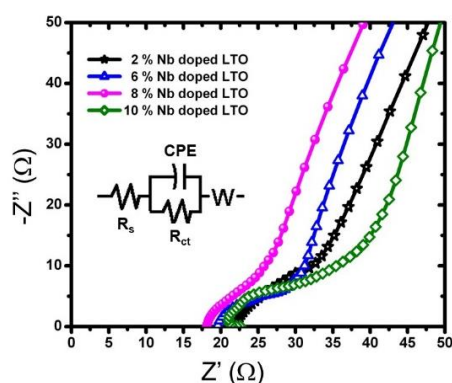


Figure 13. The Nyquist plots of $\text{Li}_4\text{Ti}_{5-x}\text{Nb}_x\text{O}_{12}$ ($0.02 \leq x \leq 0.10$) electrodes.

Table 1. Results of the EIS fitting.

x (Nb)	R_s (Ω)	R_{ct} (Ω)	CPE (μF)	σ_w ($\Omega \text{ s}^{-1/2}$)
0.00	31.0	63.8	1.56	4.67
0.02	22.5	12.5	3.21	4.71
0.06	19.0	12.1	4.03	4.72
0.08	18.1	5.3	8.22	4.80
0.10	21.6	15.8	6.01	5.11

4. Discussion

In this study, we have shown that niobium doping in $\text{Li}_4\text{Ti}_{5-x}\text{Nb}_x\text{O}_{12}$ in the compositional range $0.02 \leq x \leq 0.10$ does not affect the structural properties of the LTO electrode. All compounds have crystallite size of ~ 40 nm and crystallize with cubical morphology. The partial substitution of Nb for Ti only slightly increases the unit cell volume and enhances the electrical conductivity of the spinel lattice as expected. The electrochemical capacitance, cycle stability, and Nyquist data confirm a decrease in the charge transfer resistance and an increase in the electrical conductivity. The small lattice expansion probably does not create large free 3D channels for enhancing the lithium ions' transport during the insertion–extraction reactions. However, a significant increase in the electrical conductivity (by almost three orders of magnitude) has been observed. Wolfenstine and Allen [51] reported that the DC electronic conductivity of $\text{Li}_4\text{Ti}_5\text{O}_{12}$ increased from $\sim 8 \times 10^{-10}$ to $\sim 1 \times 10^{-9}$ S cm^{-1} when doped with 5% Ta. Similarly, Zhang et al. [52] show that the substitution of W^{6+} ions for Ti^{4+} ions in the structure, i.e., $\text{Li}_4\text{Ti}_{5-x}\text{W}_x\text{O}_{12}$ increases the conductivity by several orders of magnitude from $\sigma \approx 10^{-13}$ S cm^{-1} (pristine LTO) to $\sigma = 1.5 \times 10^{-1}$ S cm^{-1} ($\text{Li}_4\text{Ti}_{4.9}\text{W}_{0.1}\text{O}_{12}$) but with a slight sacrifice of capacity at low C-rate. Tian et al. [41] shows that the conductivity of $\text{Li}_4\text{Ti}_{4.95}\text{Nb}_{0.05}\text{O}_{12}$ and $\text{Li}_4\text{Ti}_5\text{O}_{12}$ prepared by the sol-gel method is 1.127×10^{-9} and 6.615×10^{-10} S cm^{-1} , respectively. Kim et al. [53] did not observe a significant modification of the Li-ion diffusion coefficient, \tilde{D}_{Li} , in Nb_2O_5 -doped LTO. In contrast, Yi et al. [42] reported \tilde{D}_{Li} values of 3×10^{-17} and 1.3×10^{-16} $\text{cm}^2 \text{s}^{-1}$ for $\text{Li}_4\text{Ti}_5\text{O}_{12}$ and $\text{Li}_4\text{Ti}_{4.95}\text{Nb}_{0.05}\text{O}_{12}$, respectively.

In the current study, the effect of Nb^{5+} doping in LTO materials was investigated for high-performance supercapacitors in depth. The pentavalent donor-type doping is needed to improve the electrical conductivity of the material, and Nb^{5+} ions can effortlessly substitute Ti^{4+} in the lattice of $\text{Li}_4\text{Ti}_5\text{O}_{12}$ in an extensive series of concentrations. From the experimental results, the crystal size, phase purity, inter-planar distance, etc., are parameters, which are effectively dependent on the doping level of Nb. As a result, the 8%Nb-doped LTO had better electrochemical activity than others due to its small particle size, high conductivity, and good ion diffusivity associated with the increased lattice parameters. It is obvious that 10%-Nb doping in LTO has a negative impact on the lithiation process since the conduction band is filled with more n-type Nb^{5+} ions and the number of electroactive Ti^{4+} centers are diminished. According to the results, adding a small amount of Nb to the substance could theoretically improve its overall performance by enhancing its metallic-like character, while having slight effects on its electrochemical properties. Contrastingly, a higher concentration of Nb may lead to poor electrochemical efficiency. From the CV and GCD studies, it can be concluded that the 8%Nb-doped LTO demonstrated both faradaic and capacitive storage mechanisms. On the surface of the electrodes, faradaic and capacitive processes occurred at Nb-doped centers and Ti sites, respectively. As a result, Nb^{5+} ions increase the electrical conductivity and charge storage of the working electrode.

According to the EIS results from Figure 13, the comparison of the low-frequency range corresponding to the ionic conductivity does not show a significant change between the 8%Nb-doped LTO and pristine LTO sample. This indicates that the concentration of Li vacancies (as expected for an increase in the Li-ion diffusion) is not changed in the doped-LTO structure. The large increase in the electronic conductivity from 4.6×10^{-9} S cm^{-1} (pure LTO) to 2.37×10^{-6} S cm^{-1} ($\text{Li}_4\text{Ti}_{4.92}\text{Nb}_{0.08}\text{O}_{12}$) is due to a charge compensation by a Ti vacancy given in Equation (3):

$$4[\text{V}^{\text{Ti}}] = [\text{Nb}_{\text{Ti}}^{\bullet}] \quad (3)$$

and the defect model is of the form $[\text{Li}]_{8a}[\text{Li}_{1/3}\text{Ti}_{5/3-y}\text{Nb}_{y/5}\text{V}_{4y/5}^{\text{Ti}}]_{16d}\text{O}_4$.

For the first time, the capacitive properties of $\text{Li}_4\text{Ti}_{5-x}\text{Nb}_x\text{O}_{12}$ have been investigated. The specific capacitance of the 8%Nb-doped LTO anode material is 497 F g^{-1} after 5000 charge–discharge cycles at a current rate of 1 A g^{-1} (or 6C rate) and a specific discharge capacity of 111.1 mAh g^{-1} at current density of 2 A g^{-1} . A comparison of our results with

the electrochemical properties of doped LTO electrodes (i.e., energy density, power density) reported in the literature is reported in Table 2. In terms of capacity (mAh g^{-1}) or capacitance (F g^{-1}), these electrodes include AC/LTO ($\sim 45 \text{ mAh g}^{-1}$) [54], 80LFP-20AC/LTO ($\sim 70 \text{ mAh g}^{-1}$) [54], AC/LTO (27 mAh g^{-1}) [37], LTO/graphene (207 F g^{-1}) [39], sol-gel prepared LTO (103 mAh g^{-1} at 0.1C) [34], pre-lithiated LTO (79 mAh g^{-1} at 0.2C) [35], porous LTO granules (43 F g^{-1} at 0.8 A g^{-1} rate) [36]. As a result, the discharge rate of the 8%Nb-doped LTO is faster than that of the nanostructured LTO materials reported so far, emphasizing a great promise of the Nb-doped intercalation-type material for high-energy and high-power asymmetric supercapacitor applications.

Table 2. Comparative study of the electrochemical performance of LTO-based anode for pseudocapacitor.

Material	Synthesis	Energy Density (Wh kg^{-1})	Power Density (kW kg^{-1})	Ref.
LTO/AC	Solid-state reaction	24	0.12	[55]
TiO ₂ -decorated LTO	Hydrothermal	75.8	0.3	[56]
LTO/AC nanotubes	In-situ sol gel	32	6	[57]
LTO/MWCNT	Spray drying	70.9	0.03	[33]
LTO nanoparticles	Hydrothermal	10	0.2	[58]
C-coated LTO	Hydrothermal	30	0.1	[59]
LTO	Wet chemistry	50	0.3	[60]
LTO	Solid-state reaction	45.5	0.76	[39]
Mg-doped LTO	Solid-state reaction	47.8	0.77	[39]
Mn-doped LTO	Solid-state reaction	52.3	0.85	[39]
V-doped LTO	Solid-state reaction	58.2	0.83	[39]
8%Nb-doped LTO	Solid-state route	68.3	0.8	this work

5. Conclusions

Niobium-doped (2–10 mol%) nanocrystalline $\text{Li}_4\text{Ti}_5\text{O}_{12}$ electrodes were successfully synthesized by solid-state reaction with a sintering temperature of 900°C . The microstructural and elemental compositions of the synthesized electrodes were analyzed using XRD, SEM, HRTEM, Raman, and EDS, respectively. A single spinel phase (cubic $Fd3m$ structure) remains in $\text{Li}_4\text{Ti}_{5-x}\text{Nb}_x\text{O}_{12}$ doped with Nb in the range $0.02 \leq x \leq 0.08$. The (111) peak shift to lower 2θ angles indicates a marginal increase in the lattice parameter and elementary volume. SEM and TEM images displayed homogeneously distributed cubical grains with size of nanometer range. The particle size of 8%Nb-doped LTO electrodes is found in the range of 200–250 nm. The EDS spectra and elemental mappings show the presence of Ti, O, and Nb with stoichiometric ratios in the prepared electrodes. The Raman spectrum of 8%Nb-doped LTO displayed six Raman active modes with a small red shift in Li–O and no change in O–Ti–O bonds. The electrochemical performance of the synthesized Nb-doped LTO electrodes studied using CV, GCD, and EIS techniques shows that the optimized $\text{Li}_4\text{Ti}_{4.92}\text{Nb}_{0.08}\text{O}_{12}$ sample exhibited a pseudocapacitive behavior. This electrode delivers a specific capacitance of 497 F g^{-1} at a current density of 1 A g^{-1} with 92.3% capacitance retention after 5000 cycles. Hence, $\text{Li}_4\text{Ti}_{4.92}\text{Nb}_{0.08}\text{O}_{12}$ is a promising material as an electrode for pseudocapacitive applications.

Supplementary Materials: The following are available online at <https://www.mdpi.com/article/10.3390/micro1010004/s1>, Table S1: The lattice parameters of the $\text{Li}_4\text{Ti}_{5-x}\text{Nb}_x\text{O}_{12}$ samples synthesized by solid-state reaction at 900°C ; Table S2: Results of the Rietveld refinement for pristine LTO and 8%Nb-doped LTO; Figure S1: Electrochemical performance of the $\text{Li}_4\text{Ti}_{4.94}\text{Nb}_{0.06}\text{O}_{12}$ sample: (a) CV curves of at various scan rates ($5\text{--}100 \text{ mV s}^{-1}$), (b) CV curve recorded at a scan rate of 5 mV s^{-1} showing the faradaic contribution, (c) GCD curves recorded at a current density of 2 A g^{-1} showing the faradaic voltage plateau; Figure S2: Composition dependence of the specific capacity and coulombic efficiency of $\text{Li}_4\text{Ti}_{5-x}\text{Nb}_x\text{O}_{12}$ samples measured at a current density of 2 A g^{-1} .

Author Contributions: Conceptualization, O.M.H.; investigation, J.C. and M.D.; writing—review and editing, A.M. and C.M.J.; supervision, O.M.H. All authors have read and agreed to the published version of the manuscript.

Funding: This research received no external funding.

Institutional Review Board Statement: No applicable.

Informed Consent Statement: Not applicable.

Data Availability Statement: Data are contained within the article or supplementary material.

Conflicts of Interest: The authors declare no conflict of interest.

References

1. Augustyn, V.; Simon, P.; Dunn, B. Pseudocapacitive oxide materials for high-rate electrochemical energy storage. *Energy Environ. Sci.* **2014**, *7*, 1597–1614. [[CrossRef](#)]
2. Sharma, K.; Arora, A.; Tripathi, S.K. Review of supercapacitors: Materials and devices. *J. Energy Storage* **2019**, *21*, 801–825.
3. Dhananjaya, M.; Guruprakash, N.; Lakshmi Narayana, A.; Hussain, O.M. Microstructural and supercapacitive properties of one-dimensional vanadium pentoxide nanowires synthesized by hydrothermal method. *Appl. Phys. A* **2018**, *124*, 185. [[CrossRef](#)]
4. Dhananjaya, M.; Lakshmi Narayana, A.; Guruprakash, N.; Rosaiah, P.; Hussain, O.M. Intertwining network structured V_nO_{2n+1} -CNT/GO nanocomposite electrodes for supercapacitors. *Mater. Chem. Phys.* **2019**, *237*, 121825. [[CrossRef](#)]
5. Guruprakash, N.; Dhananjaya, M.; Lakshmi Narayana, A.; Hussain, O.M. One-dimensional MoO_3 /Pd nanocomposite electrodes for high performance supercapacitors. *Mater. Res. Express* **2019**, *6*, 085543. [[CrossRef](#)]
6. Rosaiah, P.; Zhu, J.; Hussain, O.M.; Qiu, Y. Synthesis of flower-like reduced graphene oxide- Mn_3O_4 nanocomposite electrodes for supercapacitors. *Appl. Phys. A* **2018**, *124*, 597. [[CrossRef](#)]
7. Lakshmi Narayana, A.; Dhananjaya, M.; Guruprakash, N.; Hussain, O.M.; Julien, C.M. Nanocrystalline Li_2TiO_3 electrodes for supercapattery application. *Ionics* **2017**, *23*, 3419–3428. [[CrossRef](#)]
8. Dhananjaya, M.; Guruprakash, N.; Lakshmi Narayana, A.; Hussain, O.M. Electrochemical performance of nanocrystalline vanadium pentoxide thin films grown by RF magnetron sputtering. *J. Electron. Mater.* **2020**, *49*, 1922–1934. [[CrossRef](#)]
9. Winter, M.; Brodd, R.J. What are batteries, fuel cells, and supercapacitors? *Chem. Rev.* **2004**, *104*, 4245–4269. [[CrossRef](#)]
10. Chen, G.Z. Understanding supercapacitors based on nanohybrid materials with interfacial conjugation. *Prog. Nat. Sci. Mater. Int.* **2013**, *23*, 245–255. [[CrossRef](#)]
11. Jin, S.; Lee, H.; Yim, S. Enhanced capacitive properties of all-metal-oxide-nanoparticle-based asymmetric supercapacitors. *RSC Adv.* **2019**, *9*, 31846–31852. [[CrossRef](#)]
12. Jezowski, P.; Crosnier, O.; Brousse, T. Sodium borohydride ($NaBH_4$) as a high-capacity material for next generation sodium-ion. *Open Chem.* **2021**, *19*, 432–441. [[CrossRef](#)]
13. Chandra-Sekhar, J.; Dhananjaya, M.; Hussain, O.M. Microstructural and supercapacitive performance of cubic spinel $Li_4Ti_5O_{12}$ nanocomposite. *Eur. J. Mater. Sci. Eng.* **2020**, *5*, 222–233.
14. Rho, Y.H.; Kanamura, K. Li^+ ion diffusion in $Li_4Ti_5O_{12}$ thin film electrode prepared by PVP sol-gel method. *J. Solid State Chem.* **2004**, *177*, 2094–2100. [[CrossRef](#)]
15. Michalska, M.; Lemanski, K.; Ptak, M.; Roguska, A.; Chernyayeva, O.; Zurek, P.; Sikora, A.; Golebiewski, P.; Szysiak, A.; Malinowska, A.; et al. Effects of Eu^{3+} ions doping on physicochemical properties of spinel-structured lithium-titanium oxide ($Li_4Ti_5O_{12}$) as an efficient photoluminescent material. *Mater. Res. Bull.* **2021**, *134*, 111084. [[CrossRef](#)]
16. Shi, L.; Hu, X.; Huang, Y. Fast microwave-assisted synthesis of Nb-doped $Li_4Ti_5O_{12}$ for high-rate lithium-ion batteries. *J. Nanopart. Res.* **2014**, *16*, 2332. [[CrossRef](#)]
17. Yang, C.-C.; Hu, H.-C.; Lin, S.J.; Chien, W.-C. Electrochemical performance of V-doped spinel $Li_4Ti_5O_{12}$ /C composite anode in Li-half and $Li_4Ti_5O_{12}$ /LiFePO₄-full cell. *J. Power Sources* **2014**, *258*, 424–433. [[CrossRef](#)]
18. Xue, X.; Yan, H.; Fu, Y. Preparation of pure and metal-doped $Li_4Ti_5O_{12}$ composites and their lithium-storage performances for lithium-ion batteries. *Solid State Ion.* **2019**, *335*, 1–6. [[CrossRef](#)]
19. Rahman, M.M.; Wang, J.-Z.; Hussain, M.F.; Wexler, D.; Liu, H.K. Amorphous carbon coated high grain boundary density dual phase $Li_4Ti_5O_{12}$ /TiO₂: A nanocomposite anode material for Li-ion batteries. *Adv. Energy Mater.* **2011**, *1*, 212–220. [[CrossRef](#)]
20. Choi, H.S.; Kim, T.H.; Im, J.H.; Park, C.R. Preparation and electrochemical performance of hyper-networked $Li_4Ti_5O_{12}$ /carbon hybrid nanofiber sheets for a battery-supercapacitor hybrid system. *Nanotechnology* **2011**, *22*, 405402. [[CrossRef](#)]
21. Zhao, B.; Deng, X.; Ran, R.; Liu, M.; Shao, Z. Facile synthesis of a 3D nanoarchitected $Li_4Ti_5O_{12}$ electrode for ultrafast energy storage. *Adv. Energy Mater.* **2016**, *6*, 1500924. [[CrossRef](#)]
22. Dong, S.; Wang, X.; Shen, L.; Li, H.; Wang, J.; Nie, P.; Wang, J.; Zhang, X. Trivalent Ti self-doped $Li_4Ti_5O_{12}$: A high performance anode material for lithium-ion capacitors. *J. Electroanal. Chem.* **2015**, *757*, 1–7. [[CrossRef](#)]
23. Hao, Y.-J.; Lai, Q.-Y.; Lu, J.-Z.; Ji, X.-Y. Effects of dopant on the electrochemical properties of $Li_4Ti_5O_{12}$ anode materials. *Ionics* **2007**, *13*, 369–373. [[CrossRef](#)]

24. Tian, S.; Wang, X.; Yang, J. Enhanced lithium-storage performance of $\text{Li}_4\text{Ti}_5\text{O}_{12}$ coated with boron-doped carbon layer for rechargeable Li-ion batteries. *Solid State Ion.* **2018**, *324*, 191–195. [[CrossRef](#)]
25. Karhunen, T.; Valikangas, J.; Torvela, T.; Lahde, A.; Lassi, U.; Jokiniemi, J. Effect of doping and crystallite size on the electrochemical performance of $\text{Li}_4\text{Ti}_5\text{O}_{12}$. *J. Alloys Compd.* **2016**, *659*, 132–137. [[CrossRef](#)]
26. Liang, Q.; Cao, N.; Song, Z.; Gao, X.; Hou, L.; Guo, T.; Qin, X. Co-doped $\text{Li}_4\text{Ti}_5\text{O}_{12}$ nanosheets with enhanced rate performance for lithium-ion batteries. *Electrochim. Acta* **2017**, *251*, 407–414. [[CrossRef](#)]
27. Ming, H.; Ming, J.; Li, X.; Zhou, Q.; Wang, H.; Jin, L.; Fu, Y.; Adkins, J.; Zheng, J. Hierarchical $\text{Li}_4\text{Ti}_5\text{O}_{12}$ particles co-modified with C&N towards enhanced performance in lithium-ion battery applications. *Electrochim. Acta* **2014**, *116*, 224–229.
28. Sohib, A.; Priyono, S.; Widayatno, W.B.; Subhan, A.; Sari, S.N.; Wismogroho, A.S.; Hudaya, C.; Prihandoko, B. Electrochemical performance of low concentration Al doped-lithium titanate anode synthesized via sol-gel for lithium ion capacitor applications. *J. Energy Storage* **2020**, *29*, 101480. [[CrossRef](#)]
29. Ji, M.; Xu, Y.; Zhao, Z.; Zhang, H.; Liu, D.; Zhao, C.; Qian, X.; Zhao, C. Preparation and electrochemical performance of La^{3+} and F^- co-doped $\text{Li}_4\text{Ti}_5\text{O}_{12}$ anode material for lithium-ion batteries. *J. Power Sources* **2014**, *263*, 296–303. [[CrossRef](#)]
30. Tian, B.; Xiang, H.; Zhang, L.; Wang, H. Effect of Nb-doping on electrochemical stability of $\text{Li}_4\text{Ti}_5\text{O}_{12}$ discharged to 0 V. *J. Solid State Electrochem.* **2012**, *16*, 205–211. [[CrossRef](#)]
31. Jeong, E.D.; Han, H.J.; Jung, O.S.; Ha, M.G.; Doh, C.H.; Hwang, M.J.; Yang, H.-S.; Hong, K.S. Characterizations and electrochemical performance of pure and metal-doped $\text{Li}_4\text{Ti}_5\text{O}_{12}$ for anode materials of lithium-ion batteries. *Mater. Res. Bull.* **2012**, *47*, 2847–2850. [[CrossRef](#)]
32. Zhao, E.; Qin, C.; Jung, H.-R.; Berdichevsky, G.; Nese, A.; Marder, S.; Yushin, G. Lithium titanate confined in carbon nanopores for asymmetric supercapacitors. *ACS Nano* **2016**, *10*, 3977–3984. [[CrossRef](#)]
33. Lee, G.-W.; Kim, M.-S.; Jeong, J.H.; Roh, H.-K.; Roh, K.C.; Kim, K.-B. Comparative study of $\text{Li}_4\text{Ti}_5\text{O}_{12}$ composites prepared with pristine, oxidized, and surfactant-treated multiwalled carbon nanotubes for high-power hybrid supercapacitors. *ChemElectroChem* **2018**, *5*, 2357–2365. [[CrossRef](#)]
34. Yang, J.-J.; Choi, C.-H.; Seo, H.-B.; Kim, H.-J.; Park, S.-G. Voltage characteristics and capacitance balancing for $\text{Li}_4\text{Ti}_5\text{O}_{12}$ /activated carbon hybrid capacitors. *Electrochim. Acta* **2012**, *86*, 277–281. [[CrossRef](#)]
35. Xu, N.; Sun, X.; Zhao, F.; Jin, X.; Zhang, X.; Wang, K.; Huang, K.; Ma, Y. The role of pre-lithiated in activated carbon/ $\text{Li}_4\text{Ti}_5\text{O}_{12}$ asymmetric capacitors. *Electrochim. Acta* **2017**, *236*, 443–450. [[CrossRef](#)]
36. Lee, B.-G.; Lee, S.-H. Application of hybrid supercapacitor using granule $\text{Li}_4\text{Ti}_5\text{O}_{12}$ /activated carbon with variation of current density. *J. Power Sources* **2017**, *343*, 545–549. [[CrossRef](#)]
37. Hu, X.-B.; Huai, Y.-J.; Lin, Z.-J.; Suo, J.-S.; Deng, Z.-H. A $(\text{LiFePO}_4\text{-AC})/\text{Li}_4\text{Ti}_5\text{O}_{12}$ hybrid battery capacitor. *J. Electrochem. Soc.* **2007**, *154*, A1026–A1030. [[CrossRef](#)]
38. Lee, B.; Yoon, J.R. Preparation and characteristics of $\text{Li}_4\text{Ti}_5\text{O}_{12}$ with various dopants as anode electrode for hybrid supercapacitor. *Current Appl. Phys.* **2013**, *13*, 1350–1353. [[CrossRef](#)]
39. Khairy, M.; Faisal, K.; Mousa, M.A. High-performance hybrid supercapacitor based on pure and doped $\text{Li}_4\text{Ti}_5\text{O}_{12}$ and graphene. *J. Solid State Electrochem.* **2017**, *21*, 873–882. [[CrossRef](#)]
40. Sarantuya, L.; Tsogbadrakh, N.; Sevjiduren, G.; Altantsog, P. Carrier and transition metals (M = Nb, Cr and Fe) doping effects on structure and electronic structure in spinel $\text{Li}_4\text{Ti}_5\text{O}_{12}$ compounds. *Solid State Phenom.* **2020**, *310*, 88–95. [[CrossRef](#)]
41. Tian, B.; Xiang, H.; Zhang, L.; Li, Z.; Wang, H. Niobium doped lithium titanate as a high rate anode material for Li-ion batteries. *Electrochim. Acta* **2010**, *55*, 5453–5458. [[CrossRef](#)]
42. Yi, T.-F.; Xie, Y.; Shu, J.; Wang, Z.; Yue, C.-B.; Zhu, R.-S.; Qiao, H.-B. Structure and electrochemical performance of niobium-substituted spinel lithium titanium oxide synthesized by solid-state method. *J. Electrochem. Soc.* **2011**, *158*, A266–A274. [[CrossRef](#)]
43. Jezowski, P.; Kowalczewski, P.L. Starch as a green binder for the formulation of conducting glue in supercapacitors. *Polymers* **2019**, *11*, 1648. [[CrossRef](#)]
44. Lee, S.C.; Lee, S.M.; Lee, J.W.; Lee, J.B.; Lee, S.M.; Han, S.S.; Lee, H.C.; Kim, H.J. Spinel $\text{Li}_4\text{Ti}_5\text{O}_{12}$ nanotubes for energy storage materials. *J. Phys. Chem. C* **2009**, *113*, 18420–18423. [[CrossRef](#)]
45. Vikram-Babu, B.; Sushma-Reddi, M.; Surendra, K.; Rama-Krishna, A.; Samatha, K.; Veeraiah, V. Synthesis, characterization and electrical studies of Nb-substituted $\text{Li}_4\text{Ti}_5\text{O}_{12}$ anode materials for Li-ion batteries. *Mater. Today Proc.* **2020**, *43*, 1485–1490. [[CrossRef](#)]
46. Nagarani, N. Structural and optical characterization of ZnO thin films by sol-gel method. *J. Phot. Spintron.* **2013**, *2*, 19–21.
47. Julien, C.M.; Zaghib, K. Electrochemistry and local structure of nano-sized $\text{Li}_{4/3}\text{Me}_{5/3}\text{O}_4$ (Me = Mn, Ti) spinels. *Electrochim. Acta* **2004**, *50*, 411–416. [[CrossRef](#)]
48. Jiang, Y.; Liu, J. Definitions of pseudocapacitive materials: A brief review. *Energy Environ. Mater.* **2019**, *2*, 30–37. [[CrossRef](#)]
49. Wang, J.; Polleux, J.; Lim, J.; Dunn, B. Pseudocapacitive contributions to electrochemical energy storage in TiO_2 (anatase) nanoparticles. *J. Phys. Chem. C* **2007**, *111*, 14925–14931. [[CrossRef](#)]
50. Song, Y.; Pan, Q.; Lv, H.; Yang, D.; Qin, Z.; Zhang, M.; Sun, X.; Liu, X. Ammonium-ion storage using electrodeposited manganese oxides. *Angew. Chem.* **2021**, *60*, 5718–5722. [[CrossRef](#)] [[PubMed](#)]
51. Wolfenstine, J.; Allen, J.L. Electrical conductivity and charge compensation in Ta doped $\text{Li}_4\text{Ti}_5\text{O}_{12}$. *J. Power Sources* **2008**, *180*, 582–585. [[CrossRef](#)]

52. Zhang, Q.Y.; Zhang, C.L.; Li, B.; Jiang, D.D.; Kang, S.F.; Li, X.; Wang, Y.G. Preparation and characterization of W-doped $\text{Li}_4\text{Ti}_5\text{O}_{12}$ anode material for enhancing the high rate performance. *Electrochim. Acta* **2013**, *107*, 139–146. [[CrossRef](#)]
53. Kim, S.-K.; Kwon, E.-S.; Kim, T.-H.; Moon, J.; Kim, J. Effects of atmospheric Ti (III) reduction on Nb_2O_5 -doped $\text{Li}_4\text{Ti}_5\text{O}_{12}$ anode materials for lithium ion batteries. *Ceram. Int.* **2014**, *40*, 8869–8874. [[CrossRef](#)]
54. Chen, S.; Hu, H.; Wang, C.; Wang, G.; Yin, J.; Cao, D. $(\text{LiFePO}_4\text{-AC})/\text{Li}_4\text{Ti}_5\text{O}_{12}$ hybrid supercapacitor: The effect of LiFePO_4 content on its performance. *J. Renew. Sustain. Energy* **2012**, *4*, 033114. [[CrossRef](#)]
55. Dabonot, A.; Mailley, S.; Azaïs, P.; Mailley, P.; Dagorne-Gutel, E. Hybrid supercapacitors including a $\text{Li}_4\text{Ti}_5\text{O}_{12}$ /activated carbon composite negative electrode. In *Electrochemical Society Meeting Abstracts 223*; The Electrochemical Society, Inc.: Philadelphia, PA, USA, 2013.
56. Gao, L.; Huang, D.; Shen, Y.; Wang, M. Rutile- TiO_2 decorated $\text{Li}_4\text{Ti}_5\text{O}_{12}$ nanosheet arrays with 3D interconnected architecture as anodes for high performance hybrid supercapacitors. *J. Mater. Chem. A* **2015**, *3*, 23570–23576. [[CrossRef](#)]
57. Choi, H.S.; Im, J.H.; Kim, T.-H.; Park, J.H.; Park, C.R. Advanced energy storage: A hybrid BatCap system consisting of battery-supercapacitor hybrid electrodes based on $\text{Li}_4\text{Ti}_5\text{O}_{12}$ -activated-carbon hybrid nanotubes. *J. Mater. Chem.* **2012**, *12*, 16986–16993. [[CrossRef](#)]
58. Du Pasquier, A.; Laforgue, A.; Simon, P. $\text{Li}_4\text{Ti}_5\text{O}_{12}$ /poly(methyl)thiophene asymmetric hybrid electrochemical device. *J. Power Sources* **2004**, *125*, 95–102. [[CrossRef](#)]
59. Jung, H.-G.; Venugopal, N.; Scrosati, B.; Sun, Y.-K. A high energy and power density hybrid supercapacitor based on an advanced carbon-coated $\text{Li}_4\text{Ti}_5\text{O}_{12}$ electrode. *J. Power Sources* **2013**, *221*, 266–271. [[CrossRef](#)]
60. Dsoke, S.; Fuchs, B.; Gucciardi, E.; Wohlfahrt-Mehrens, M. The importance of the electrode mass ratio in a Li-ion capacitor based on activated carbon and $\text{Li}_4\text{Ti}_5\text{O}_{12}$. *J. Power Sources* **2015**, *282*, 385–393. [[CrossRef](#)]